JOURNAL OF GEOPHYSICAL RESEARCH, VOL. 103, NO. C2, PAGES 2945–2961, FEBRUARY 15, 1998

Numerical simulations of the baroclinic dynamics of density-driven coupled fronts and eddies on a sloping bottom

Gordon E. Swaters

Department of Mathematical Sciences, Applied Mathematics Institute, and Institute of Geophysics, Meteorology and Space Physics, University of Alberta, Edmonton, Canada

Abstract. Numerical simulations of the baroclinic dynamics of density-driven coupled fronts and eddies are described. The simulations are based on a two-layer intermediate length scale model which filters out barotropic instability and focuses on the subinertial baroclinic evolution of density-driven flows within the context of allowing finite-amplitude height variations in the lower layer. The baroclinic destabilization of a bottom-trapped coupled front on a sloping bottom is described. In the overlying fluid the instability takes the form of amplifying topographic Rossby waves. In the coupled front the perturbations to the downslope incropping are preferentially amplified compared to those on the upslope incropping. The perturbations to the downslope incropping develop into downslope propagating plumes which eventually evolve into relatively coherent along-slope propagating domes. We discuss the propagation characteristics of these domes. We also simulate the evolution of density-driven eddies or domes. The first eddy simulation we describe is for an initial eddy configuration which satisfies a zero topographic Rossby wave condition in the upper layer. We show that these traveling solutions remain remarkably coherent over a period of about 40 eddy circulation times or about 250 days for typical continental slope values. For a sufficiently large initial eddy height, upper layer fluid parcels can be transported in the along-slope direction by the baroclinic eddy. We also simulate the evolution of an initial eddy configuration which does not satisfy a zero topographic Rossby wave condition in the upper layer. A relatively intense cyclonic circulation develops in the overlying fluid over the traveling dome as does a topographic Rossby wave tail. However, even these solutions remain surprisingly coherent over many eddy circulation times.

1. Introduction and Model Description

When large-scale plumes of dense water are released into a shallow sea, such as a shelf region, and settle onto the bottom, the combined influences of the Coriolis and buoyancy stresses may force the plume to be transversely constrained and flow, in the northern hemisphere, with the direction of locally increasing bottom height to its right. Because these geostrophically balanced flows on a sloping bottom are driven by the density contrast between the relatively dense plume and the surrounding water we refer to them as "mesoscale gravity currents" [see, e.g., *Britter and Linden*, 1980; *Honji and Hosoyamada*, 1989; *LeBlond et al.*, 1991] in order to emphasize the underlying fluid dynamical configuration and to differentiate them from non-rotating gravity currents on a flat bottom. Examples include the Denmark Strait overflow [*Smith*, 1976], the migration of Antarctic Bottom Water [*Whitehead and Worthington*, 1982], deep water formation in the Adriatic Sea [*Zoccolotti and Salusti*, 1987], and deep water replacement in the Strait of Georgia [*LeBlond et al.*, 1991]. The formation of bottom-trapped propagating cold eddies or domes (e.g., *Armi and D'Asaro* [1980], *Houghton et al.* [1982], *Mory et al.* [1987], *Nof* [1983], and *Swaters and Flierl* [1991], among others) may be the result of the instability of these currents.

Griffiths et al. [1982] (hereinafter referred to as GKS) developed a low-wavenumber stability analysis of a mesoscale gravity current based on a reduced-gravity model. When GKS compared the predictions of their theory to laboratory experiments of the instability of a buoyant coupled front, substantial differences were found. For example, the unstable modes described by GKS had asymptotically small along-front wavenumbers while the observed instabilities occurred over a range of wavenumbers including those corresponding to finite wavelengths. Another difficulty with the theory was that the observed instability had a dominant length scale independent of the current width in contradiction to the theoretical prediction. A third aspect of the observations that the theory could not explain was a secondary branch of instabilities which had a dipole-like appearance. This difference was attributed to the existence of another, possibly baroclinic, unstable mode outside the range of applicability of the GKS analysis.

In part to address these issues, *Swaters* [1991] developed an "intermediate length scale" [see, e.g., *Charney and Flierl*, 1981] theory for the baroclinic instability of mesoscale gravity currents. This model assumed that the dynamics of the overlying water (see Figure 1) was quasi-geostrophic and driven by vortex-tube stretching and that the gravity current, while in geostrophic balance, was not quasi-geostrophic since the dynamic deflections of the current height are of the same order of magnitude as the scale height for the current. This balance represented a middle dynamical regime between full two-layer shallow water theory and the kinematic assumptions of quasi-geostrophic theory.

The instability mechanism modeled by *Swaters* [1991] is the release of the available potential energy associated with a pool of dense water sitting directly on a sloping bottom surrounded by relatively lighter water. For an unstable gravity current which has a transverse thickness profile shaped like a coupled front, the instabilities take the form of along-front traveling waves which preferentially amplify on the downslope side of the coupled front, which develop into downslope propagating plumes.

The amplifying perturbations on the upslope and downslope incroppings are asymmetric in contrast to that which would be predicted by barotropic (i.e., horizontal shear-based) instability theory [see, e.g., *Paldor and Killworth*, 1987]. This asymmetry is an unique signature of the baroclinic destabilization of these currents. From a modal point of view the instability may be thought of as the coalescence of two topographic vorticity waves [*Mooney and Swaters*, 1996; *Boss et al.*, 1996] which have been excited in the upper layer. The *Swaters* [1991] model was also able to reproduce a dipole-like instability similar to that observed by GKS. Recently, *Jiang and Garwood* [1996] concluded that the instabilities observed in three-dimensional numerical simulations of overflows on a continental slope arise because of this instability mechanism.

The *Swaters* [1991] model can be derived as a systematic asymptotic reduction of the full two-layer shallow water equations for a rotating fluid on a sloping bottom. In addition to the *Swaters* [1991] general instability calculation, this theory has been used to model the propagation of ventilated cold domes [*Swaters and Flierl*, 1991] and the stability characteristics of deep water replacement in the Strait of Georgia [*Karsten et al.*, 1995]. *Swaters* [1993] showed that the model possessed a noncanonical Hamiltonian formulation and exploited this structure to examine the nonlinear stability problem [see also *Karsten and Swaters*, 1996].

Because this model possesses both steady mesoscale gravity current (e.g., coupled front) and steadily traveling density-driven isolated eddy (i.e., cold dome) solutions, it is of interest to ask whether it is possible for the amplifying modes associated with an unstable coupled front to evolve into steadily traveling baroclinic eddies. A partial answer to this question was provided by *Mooney and Swaters* [1996], who developed a wave-packet model for marginally unstable modes of unsheared gravity current solutions of the model. Unfortunately, since the steady current was unsheared in the transverse (i.e., cross-slope) direction, at the point of marginal instability the entire flow forms a nonlinear critical layer (similar to what happens in the Phillip's model of baroclinic instability; see, e.g., *Warn and Gauthier* [1989]), and thus determining the evolution of the marginally unstable mode required solving an infinite number of coupled amplitude equations.

Mooney and Swaters [1996] were unable to find an isolated eddy-like solution to these equations, except under the ad hoc approximation of simply neglecting all harmonics save the fundamental and the principal mean flow it generates. In this case the governing amplitude equations can be transformed into a sine-Gordon equation [see, e.g., *Gibbon et al.*, 1979], which has a solitary wave solution which can be interpreted as a steadily traveling cold dome. The nonlinear analysis of more complicated unstable steady flows, such as a coupled front, and the emergence and dynamical characteristics of propagating cold domes of direct relevance to shelf dynamics can, however, be examined numerically.

The principal purpose of this paper is to present the results of direct numerical simulations of the *Swaters* [1991] model. In particular, we describe the nonlinear baroclinic evolution of an unstable coupled front and show the formation of traveling cold domes. It is important to emphasize, however, that while the strength of our model is that it explicitly focuses on the subinertial baroclinic dynamics of these flows, this is also its weakness in as much as it neglects higher-frequency, barotropic, and other dynamical processes such as lateral and bottom friction, mixing, and thermodynamic interactions between the two layers. It is hoped that the dynamics which the present model accurately reproduces will be useful in interpreting the results of more complete numerical models [e.g., *Chapman and Gawarkiewicz*, 1995; *Gawarkiewicz and Chapman*, 1995; *Jiang and Garwood*, 1995, 1996] and oceanographic and laboratory observations.

We also examine the evolution of cold domes. *Swaters and Flierl* [1991] showed that there exist exact radially symmetric isolated steadily traveling solutions to the model. These solutions, which are baroclinic analogues of the cold eddy reduced-gravity solutions found by *Nof* [1983], are isolated in the sense that the height of the cold dome has compact support and there is no topographic Rossby wave field in the upper layer. It is a straightforward application of Andrews' [1984] theorem to show that one cannot use the underlying Hamiltonian structure to prove the stability of these solutions [*Swaters*, 1993], and it is likely the case that these eddies are not stable in the sense of Liapunov, although this remains unproven. (The failure of the energy/momentum-Casimir method in the stability problem for isolated quasi-two-dimensional vortices is generic and not restricted to the present problem. Developing a general stability theory for isolated vortices, on the basis of the underlying Hamiltonian structure, remains an important unsolved problem in geophysical fluid dynamics.) Nevertheless, the numerical simulations we present show that these solutions are relatively long-lived (up to 40 eddy circulation times or of the order of 200–300 days for typical continental shelf parameter values) and remain remarkably coherent.

We also present simulations for an initial eddy configuration which does not correspond to the *Swaters and Flierl* [1991] eddy solution. As expected, these solutions rapidly develop an upper layer topographic Rossby wave field which acts to radiate energy away from the eddy. However, we show that even these solutions remain surprisingly coherent. We conclude that propagating cold domes, whether or not they initially satisfy a

Paper number 97JC02441.
0148-0227/98/97JC-02441$09.00

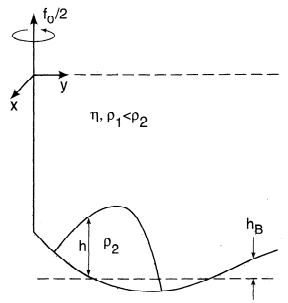

Figure 1. Geometry of the model used in this paper.

zero topographic Rossby wave condition, are robust solutions of the model and suggest that long-lived cold eddies, such as those observed by *Houghton et al.* [1982] on the New England Bight, are well described by the baroclinic dynamics of the present model.

The plan of the paper is as follows. In the remainder of this section we briefly describe the model. In section 2 we briefly outline the main stability properties associated with steady solutions of the model, which will be useful in understanding the spatial structure of the developing instabilities. In section 2 we describe our simulations for the instability problem. In section 3 we briefly outline the main features of isolated eddy solutions to the model and present our simulations for isolated and nonisolated eddy configurations. In section 4 we summarize our main conclusions.

Since the derivation of the equations has been described elsewhere [e.g., *Swaters and Flierl*, 1991; *Swaters*, 1991], our presentation will be brief. The physical geometry corresponds to a two-layer fluid (see Figure 1) on an f plane with x and y as the alongshore and offshore coordinates, respectively, and t is time. Alphabetical subscripts, except where indicated, represent partial differentiation.

If the geostrophic pressure or stream function in the upper layer is denoted by $\eta(x, y, t)$ and the lower layer current height, relative to the height of the variable bottom topography denoted by $h_B(x, y)$, is denoted as $h(x, y, t)$, then the nondimensional model can be written in the form

$$\Delta\eta_t + J(h + \eta, h_B) + J(\eta, \Delta\eta) = 0, \tag{1}$$

$$h_t + J(\eta + h_B, h) = 0, \tag{2}$$

where $J(A, B) \equiv A_xB_y - A_yB_x$. Given η and h, the velocity in the upper and lower layers and the geostrophic pressure in the lower layer are given by, respectively,

$$\mathbf{u}_1 = \hat{e}_3 \times \nabla\eta, \tag{3}$$

$$\mathbf{u}_2 = \hat{e}_3 \times \nabla(\eta + h + h_B), \tag{4}$$

$$p = h_B + \eta + h. \tag{5}$$

The nondimensionalized variables are related to the dimensional (asterisked) variables via the relations

$$(x^*, y^*) = L(x, y), \quad t^* = (sf)^{-1}t, \quad h^* = sHh,$$

$$\mathbf{u}_1^* = sfL\mathbf{u}_1, \quad \eta^* = s(fL)^2g'^{-1}\eta, \quad \mathbf{u}_2^* = sg'H(fL)^{-1}\mathbf{u}_2, \tag{6}$$

$$h_B^* = sHh_B, \qquad p^* = s\rho_2g'Hp,$$

where the horizontal length scale is the internal deformation radius $L = \sqrt{g'H}/f$ associated with the upper layer, g' is the reduced gravity, and

$$s = \frac{s^*L}{H} = \frac{s^*g'/f_0}{\sqrt{g'H}}, \tag{7}$$

is a scaled bottom slope parameter, where s^* is the unscaled bottom slope parameter and H is the mean depth of the upper layer. Equations (1) and (2) correspond to an asymptotic limit (i.e., $0 < s \ll 1$) of the full two-layer shallow water equations in which the evolution of the upper layer is quasi-geostrophic but the lower layer, while geostrophic, is not quasi-geostrophic and allows for large-amplitude thickness variations, i.e., allows for frontal configurations in which the lower layer height can intersect the bottom.

Nof [1983] showed that in the reduced gravity limit, all isolated steadily traveling eddies on a constant sloping bottom travel in the along-slope direction with speed s^*g'/f_0, which we call the Nof speed. The parameter s is the ratio of the Nof speed to the speed of long or irrotational internal gravity waves in a reduced gravity model.

The small s limit may be thought of as filtering out the higher-frequency dynamics associated with nonrotating gravity currents and focusing on the rotationally dominated aspects of the problem. Alternatively, a small s limit may be thought of as a subinertial approximation in which the horizontal length scale is larger than the internal deformation radius associated with the lower layer (i.e., an intermediate length scale approximation in the sense of, for example, *Charney and Flierl* [1981]). We also remark that while the geostrophic assumption in the cross-frontal direction in smaller-scale density-driven flows may be somewhat problematic, observations of mesoscale gravity currents [e.g., *Stacey et al.*, 1987, 1988, 1991; *LeBlond et al.*, 1991] suggest that this is an appropriate assumption.

The dimensional values associated with the above scalings depend on the local environmental parameters. For example, for the cold pool described by *Houghton et al.* [1982], the timescale is about 7 days, the horizontal length scale is about 12 km, and the lower layer velocity scale is about 2.5 cm/s [*Swaters*, 1991]. Whereas for the deep water replacement current in the Strait of Georgia, described by *LeBlond et al.* [1991], the timescale is about 11 hours, the horizontal length scale is about 7 km, and the lower layer velocity scale is about 18 cm/s [*Karsten et al.*, 1995].

From the point of view of interpreting the model in the context of potential vorticity dynamics we note that equation (1) + equation (2) is the $O(s)$ potential vorticity equation associated with the upper layer. Equation (2) is the $O(1)$ potential vorticity equation associated with the lower layer. Since the lower layer dynamics does not include inertia, we may interpret the lower layer model as a planetary geostrophic balance [see, e.g., *Pedlosky*, 1984] scaled appropriately for shelf dynamics in which the background vorticity gradient is provided by the sloping bottom. Unlike many planetary geostrophic models [e.g., *de Verdiere*, 1986], (1) and (2) do not exhibit an ultraviolet catastrophe in the instability problem.

2. Mesoscale Gravity Currents

2.1. Stability Characteristics

We first briefly describe the principal results of the linear stability theory associated with (1) and (2) as these are quite useful in interpreting the numerical simulations. For the linear stability results we assume that the domain is a channel of width l ($l \leq \infty$, we allow the possibility of an unbounded domain in the offshore direction) and that the topography only varies in the cross-channel direction, i.e., $h_B = h_B(y)$. It is straightforward to verify that $h = h_o(y)$ and $\eta = \eta_o(y)$ is an exact solution of (1) and (2) for arbitrary $h_o(y)$ and $\eta_o(y)$.

Here we choose $\eta_o = 0$ in order to focus on the purely baroclinic destabilization of a gravity current (see *Swaters* [1991, 1993] and *Karsten and Swaters* [1996] for the general stability theory). Substitution of

$$h(x, y, t) = h_o(y) + \mathrm{Re}\,\{\bar{h}(y)\exp[ik(x - ct)]\}, \tag{8}$$

$$\eta(x, y, t) = \mathrm{Re}\,\{\bar{\eta}(y)\exp[ik(x - ct)]\} \tag{9}$$

into (1) and (2) and linearizing about the mean flow $h_o(y)$ leads to the modified Raleigh-Kuo equation (after dropping the tildes)

$$\eta_{yy} - \left[k^2 + \frac{h_{B_y}}{c} + \frac{h_{B_y}h_{o_y}}{c(c + h_{B_y})}\right]\eta = 0, \tag{10}$$

$$h = \frac{h_{o_y}\eta}{(c + h_{B_y})}, \tag{11}$$

with $\eta = 0$ on the channel walls and continuously differentiable elsewhere.

The first thing to note is that sloping topography is necessary for instability; that is, without a background topographic vorticity gradient, there can be no unstable waves. This observation underscores the fact that the onset of instability occurs because of the coalescence of two topographic Rossby waves [*Mooney and Swaters*, 1996].

It follows from the y-integrated energy balance relation associated with (10) that a necessary condition for instability is that at least one value of y exists for which $h_{B_y}h_{o_y} > 0$ [see *Swaters*, 1991; *Karsten and Swaters*, 1996]. This fact explains why the instabilities preferentially amplify on the downslope side of a coupled front [see, e.g., *Swaters*, 1991, Figure 9].

Consider the situation where the bottom topography satisfies $h_{B_y} < 0$; that is, the mean depth of the fluid increases in the positive y direction. For a coupled front the necessary condition for instability is only satisfied on the downslope side of the front (where $h_{o_y} < 0$) and not on the upslope side (where $h_{o_y} > 0$). The perturbations to the incroppings preferentially amplify on the downslope side because it is only on this side that the necessary conditions for instability hold. As we shall see in the numerical simulations, the perturbations to the downslope incropping develop into downslope propagating plumes which can evolve into along-slope traveling cold domes.

It also follows from the y-integrated energy balance relation associated with (10) that $\mathrm{Re}\,(v^*h)$ must be positively correlated with $-h_{B_y}$ if instability occurs (where v is the cross-channel velocity in the upper layer and the asterisk indicates the complex conjugate, see *Swaters* [1991]). Thinking of positive h anomalies as cold anomalies in the upper layer implies that instability only occurs if there is a net transport of heat *up* the background vorticity gradient, i.e., baroclinic instability [*LeBlond and Mysak*, 1978]. The instability corresponds to the release of the (gravitational) available potential energy (APE) associated with the downslope "slumping" of the gravity current. Because of the downslope slumping associated with an unstable gravity current and the concomitant mass transport we may think of this as an convective instability. (There is nothing new in thinking of baroclinic instability as the convective instability of a rotating fluid [see, e.g., *Pedlosky*, 1987, chapter 7].)

2.2. Simulation of an Unstable Coupled Front

Equations (1) and (2) were numerically solved as the system

$$q_t + J(\eta, q + h_B) = 0, \tag{12}$$

$$h_t + J(\eta + h_B, h) = \nu\Delta h, \tag{13}$$

$$\Delta\eta = q - h, \tag{14}$$

where (12) is simply equation (1) + equation (2). Equations (12) and (13) were integrated forward in time using a 128 × 128 grid point second-order leapfrog procedure with the *Arakawa* [1966] finite difference scheme implemented for the Jacobian. A Robert filter [*Asselin*, 1972] with coefficient 0.005 was applied at each time step to suppress the computational mode. The upper layer stream function η was obtained from (14) at each time step using a direct solver. The numerical friction term Δh with coefficient $\nu = 10^{-3}$ was included in (13) to suppress high-wavenumber features in the simulations. For the gravity current simulations the equations were solved in the periodic channel

$$\Omega - \{(x, y) | |x| < 2\pi, |y| < 2\pi\}, \tag{15}$$

where the periodicity is in the x direction and we impose $\eta - 0$ on $y - \pm 2\pi$.

We did a number of simulations before deciding on the domain size. Our goal was to have a computational domain small enough that the current and any subsequent eddies which might form would be adequately resolved. At the same time, the computational domain had to be large enough so that we could have more than one wavelength associated with the most unstable mode and so that the location of the offshore computational boundary did not affect the time evolution.

The first set of simulations we describe is the destabilization of a smooth coupled front on a constant sloping bottom. The bottom topography is given by

$$h_B(y) = -(y + 2\pi). \tag{16}$$

The initial condition for the gravity current is given by

$$h(x, y, 0) = h_o(y)$$

$$= \begin{cases} \{1 + \cos[\pi(y + \frac{1}{4})]\}/2, & |y + \frac{1}{4}| \leq 1, \\ 0, & |y + \frac{1}{4}| > 1. \end{cases} \tag{17}$$

The initial lower layer height field is continuously differentiable at the incroppings; that is, $h_o = h_{o_y} = 0$ at $y = -\frac{5}{4}$ and $\frac{3}{4}$, respectively. This smoothness implies that the finite difference representation of the initialized Jacobian terms is continuous across the incroppings. The finite difference grid used implies that initially there are 20 grid points inside the coupled front in the cross-slope direction. The maximum current thickness is located at $y = -\frac{1}{4}$. This choice helps to ensure that the effect of the offshore computational boundary is minimized in the numerical integration. Another point worth making is that the initial condition for the lower layer height does not include any perturbation; that is, it does not include any contribution associated with the most unstable mode from a linear instability analysis [e.g., *Swaters*, 1991]. The destabilization will be initiated by the presence of perturbations in the upper layer.

The initial condition for the upper layer stream function, denoted as $\eta_o(x, y)$, is a band-limited linear superposition of modes, centered about the most unstable mode associated with h_o, which has an along-channel wavenumber of about 1.5, satisfying the boundary and periodicity conditions with random phase shifts and amplitudes for which the upper layer kinetic energy is 10% of the potential energy in the initialized coupled front; that is,

$$\frac{\displaystyle\int\int_\Omega \nabla\eta_o \cdot \nabla\eta_o \, dx\, dy}{\displaystyle\int\int_\Omega h_o^2 \, dx\, dy} = 10^{-1}. \tag{18}$$

The initial conditions are shown in the $t = 0$ panels in Plate 1 (a complete description of these panels is given below). The upper layer stream function is a superposition of the random modes just described, and the lower layer height does not contain any perturbations.

In Figure 2 we show the normalized area-averaged upper layer kinetic energy ⟨KE⟩, defined by

$$\langle \mathrm{KE} \rangle(t) = \frac{\displaystyle\int\int_{\Omega} \nabla\eta \cdot \nabla\eta \, dx \, dy}{\displaystyle\int\int_{\Omega} \nabla\eta_o \cdot \nabla\eta_o \, dx \, dy}, \qquad (19)$$

versus integration time. The large dots on the curve correspond to the time of the panels in Plate 1. Since in this simulation there is no initial mean flow in the upper layer, the time variability in the ⟨KE⟩ is a direct measure of the conversion of available lower layer potential energy to upper layer kinetic energy, that is, of the baroclinic instability. The kinetic energy of the upper layer perturbation field increases monotonically until about $t = 20$ after which the ⟨KE⟩ levels off with some time variability consistent with a "saturated" baroclinic instability [see, e.g., *Pedlosky*, 1987, chapter 7].

If the destabilization were to be solely described by the most unstable mode associated with linear instability theory [*Swaters*, 1991], then the ⟨KE⟩ would be proportional to the square of the time-varying normalized amplitude of the most unstable mode (it can be shown via a weakly nonlinear analysis of a marginally unstable mesoscale gravity current that there is no mean flow generated in the upper layer to second order in the normal mode amplitude, see *Mooney and Swaters* [1996]). Notwithstanding the fact that this assumption cannot be made in the numerical simulation, the initial stages of the destabilization are reasonably well described by the most unstable mode.

In Plate 1 we show the upper layer stream function and lower layer height at $t = 0$, 10, 20, and 40, respectively. The color scale for the lower layer height panels is uniform over the entire sequence with the grey through red sequence of colors corresponding to the height scale 0.0 through 1.0. Because there is considerable time variability in the range of the upper layer stream function values over time and we are mostly interested in the qualitative pattern established rather than the precise numerical values, it is more convenient to use a variable color scale which ranges from the stream function minimum to the stream function maximum in each individual panel as shown beneath the $t = 40$ stream function panel.

The left- and right-hand edge of each panel in Plate 1 corresponds to the minimum and maximum along-slope computational boundary, respectively, and the bottom and top edge in each panel corresponds to the minimum and maximum cross-slope computational boundary, respectively. Thus the along-slope, i.e., x, coordinate increases from left to right, and the downslope, i.e., y, coordinate increases from bottom to top in each panel. The mean depth of the upper layer water column is therefore increasing in the bottom to top direction in each panel.

In the $t = 10$ panel, which is early in the destabilization as suggested by Figure 2, the pattern established qualitatively resembles that which would be predicted by linear instability theory [see *Swaters*, 1991, Figure 9; *Karsten and Swaters*, 1996, Figure 7]. The random structure of the initial upper layer stream function has evolved into a pattern in which the extrema are located over the perturbed downslope incropping of the coupled front. This pattern is similar to the upper layer wave field described by *Swaters* [1991] for the most unstable mode.

The amplitude of the perturbation associated with the downslope incropping is, on average, much larger than that of the upslope incropping as predicted by linear instability theory [*Swaters*, 1991]. In a linear instability analysis, however, the perturbation amplitudes are, formally at least, infinitesimally small, and it would have been speculative to have concluded that the perturbations to the downslope incropping would evolve into finite-amplitude downslope propagating plumes.

The numerical simulations clearly show the formation of downslope propagating plumes. Even at $t = 10$ in the integration, it is still possible, qualitatively at least, to identify a dominant along-front wavenumber characteristic of a normal mode instability. The along-front power spectrum of the y-averaged perturbation fields (not shown here) has a dominant peak centered at the wavenumber of the most unstable mode (about 1.5), which is consistent with that observed in the $t = 10$ panel.

At $t = 20$, which, as suggested by Figure 2, is near the point at which the amplifying instability saturates into a quasiperiodic evolution, the downslope propagating plumes have evolved into globular or dome-like structures connected with smaller length scale filaments. It is not possible to identify a dominant along-front wavenumber. The orientation of the filaments suggest that the globular structures develop an along-slope component to their velocity, which over time becomes the dominant component of velocity (this is discussed further momentarily). We chose the width of the channel to be large enough so that there is little direct interaction between the emerging dome and the downslope computational boundary during the simulation.

By $t = 40$ the downslope plumes have evolved into isolated domes (recall the periodicity in the along-slope direction), which travel in a predominantly along-slope direction. There is some small length scale and amplitude filamentary structure evident, although, from a lower layer thickness point of view, the dominant feature is the traveling dome. Our integration did not suggest that the dome feature itself rapidly becomes unstable (i.e., a secondary instability; we discuss simulations of eddy-like solutions in the next section).

It is worth remarking that as the coupled front goes unstable, the lower layer domes have anticyclonic circulation associated with them in the interior. There is no corresponding generation of cyclonic eddies in the lower layer. Since the boundary of the lower layer current and thus the eddies which form correspond to an incropping, i.e., where $h = 0$, this asymmetry can be viewed as a simple consequence of the fact that the formation of a cyclonic eddy in the lower layer would require a negative lower layer height, which is physically unacceptable.

The emergence of relatively coherent along-slope traveling domes is interesting and suggestive of along-slope propagating domes observed on continental slopes, e.g., *Houghton et al.* [1982], rotating tank experiments, e.g., *Mory et al.* [1987], and theoretical studies, e.g., *Nof* [1983] or *Swaters and Flierl* [1991]. It is of interest therefore to try and isolate the propagation characteristics of the dome-like feature once it forms in the simulation.

We were able to more or less unambiguously and continuously track the maximum height associated with the dome seen in the $t = 40$ panel of Plate 1 from an initial time of about $t =$

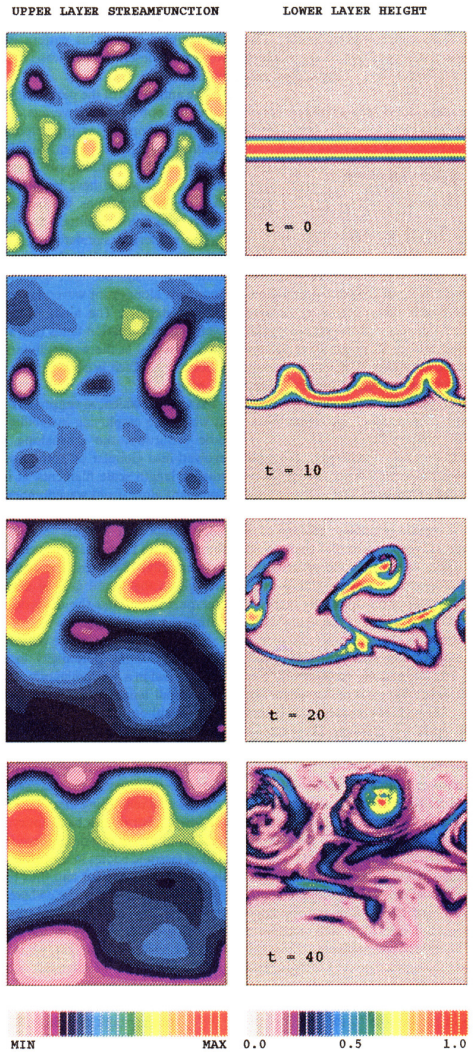

Plate 1. Sequence of panels depicting the upper layer stream function or geostrophic pressure and lower layer height for the instability simulation for $t = 0$, 10, 20, and 40, respectively. The color scale is shown underneath the $t = 40$ panels. The along-slope direction is left to right and the downslope direction is bottom to top in each panel.

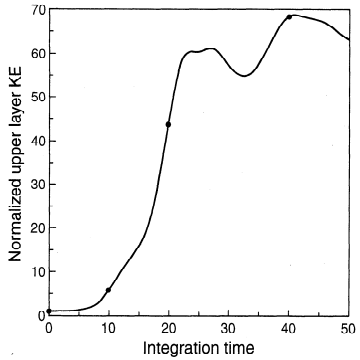

Figure 2. The area-averaged integrated upper layer kinetic energy versus the integration time normalized by its initial value for the instability simulation. The dots on the curve correspond to the integration time associated with the individual panels in Plate 1.

20 until the end of the simulation. In Figure 3 we show a scatter diagram of the path the maximum in the lower layer height field takes from $t = 20$ until the end of the simulation at $t = 40$. The maximum was initially identified by searching the lower layer numerical height array for the maximum value and then determining a precise value and location for the maximum by quadratic interpolation. In order to remove the confusion associated with the overlap of points that a scatter diagram of the trajectory in a periodic domain would have, we have added the value of the along-slope domain length (here 4π) to the along-channel coordinate of the maximum as the dome-like feature passed through the right-hand computational boundary.

Although there is some apparent irregularity in Figure 3a, which we attribute to either spurious calculation in our quadratic interpolation procedure or direct numerical integration inaccuracies, the basic pattern is clear enough. The dome follows a left-to-right along-slope trajectory which has a superimposed distinct cross-slope periodic oscillation. The amplitude of the cross-slope oscillation is relatively small with a maximum span of about one spatial unit, i.e., a deformation radius (see the length scaling in (6)).

In Figures 3b and 3c we present, respectively, scatter diagrams of the along-slope and cross-slope components of the path shown in Figure 3a as a function of time. Figure 3b suggests that the along-slope component is dominated by a rectilinear component with a small amplitude oscillation. A least squares fit of the data points in Figure 3b gives a slope of ~1.20.

For the topography given by (16), there exist isolated steadily traveling solutions to the model [*Swaters and Flierl*, 1991], which travel with the (nondimensional) *Nof* [1983] velocity (1, 0). These solutions, which we discuss more completely in the next section, have the property that there is no topographic wave field in the upper layer. We attribute the 20% difference between the observed along-slope translation speed and the theoretical Nof speed to the interaction between the topographic wave field in the upper layer and the dome-like feature in the numerical simulation, which leads to an explicit time dependence in the evolution (as suggested in Plate 1).

In Figure 3d we show a scatter diagram of the residual along-slope position, i.e., the along-slope position minus the least squares prediction of the along-slope position of the maximum dome height, in order to remove the linear trend and to illustrate the time variability in the along-slope position. If we compare Figures 3c and 3d, it appears that the cross-slope oscillation leads the along-slope oscillation by ~90° of phase or a quarter period.

The sloping bottom in this model can be interpreted as a topographic β plane. The cross-slope oscillations observed in Figure 3c are reminiscent of the oscillations described by *Killworth* [1983] and *Nof* [1984] or the oscillations seen in modon and point-vortex simulations on a β plane [e.g., *Makino et al.*, 1981; *Zabusky and McWilliams*, 1982] when the initial trajectory is not strictly zonally aligned.

However, we point out that the oscillations seen here are not the same as those described by *Nof* [1984] for cold domes. The oscillations described by Nof occur at the inertial period. These have been filtered out of our model (1) and (2). The oscillations seen here are distinctly subinertial.

We speculate that the cross-slope oscillations observed here are the result of a dynamical baroclinic interaction between the cold dome and the upper layer topographic Rossby wave field, which is excited in the instability process. This is a different dynamical process than that described by *Nof* [1984]. We have recently developed a theory for these oscillations and have submitted it for publication elsewhere.

In this simulation we have chosen the maximum initial height and width of the coupled front to be 1.0 and 2.0, respectively. The qualitative features seen in this simulation are not dramatically changed for different values of the initial height or width. *Swaters* [1991] did a parameter-sensitive analysis of the linear instability characteristics and showed that increasing the width of the initial coupled front leads to a modest decrease in the growth rate and along-front phase speed of the most unstable mode. The most important parameter determining the instability characteristics is the maximum initial height of the coupled front. Increasing the initial maximum height of the coupled front leads to an increased wavelength and growth rate of the most unstable mode.

3. Density-Driven Vortices

The emergence of a traveling cold dome in the instability simulation is interesting and suggestive of the possibility that these dome-like features can efficiently transport water parcels many deformation radii along a shelf. As mentioned previously, *Swaters and Flierl* [1991] found exact, steadily traveling solutions to the model equations (1) and (2) for constant sloping topography. These solutions are the baroclinic analogues of the equivalent-barotropic or reduced gravity solutions found by *Nof* [1983].

Assuming the scalings in (6), the reduced gravity model examined by *Nof* [1983] can be written in the form

$$s(\partial_t + \mathbf{u}_2 \cdot \nabla)\mathbf{u}_2 + \mathbf{e}_3 \times \mathbf{u}_2 = -\nabla(h - y), \tag{20}$$

$$h_t + \nabla \cdot (\mathbf{u}_2 h) = 0, \tag{21}$$

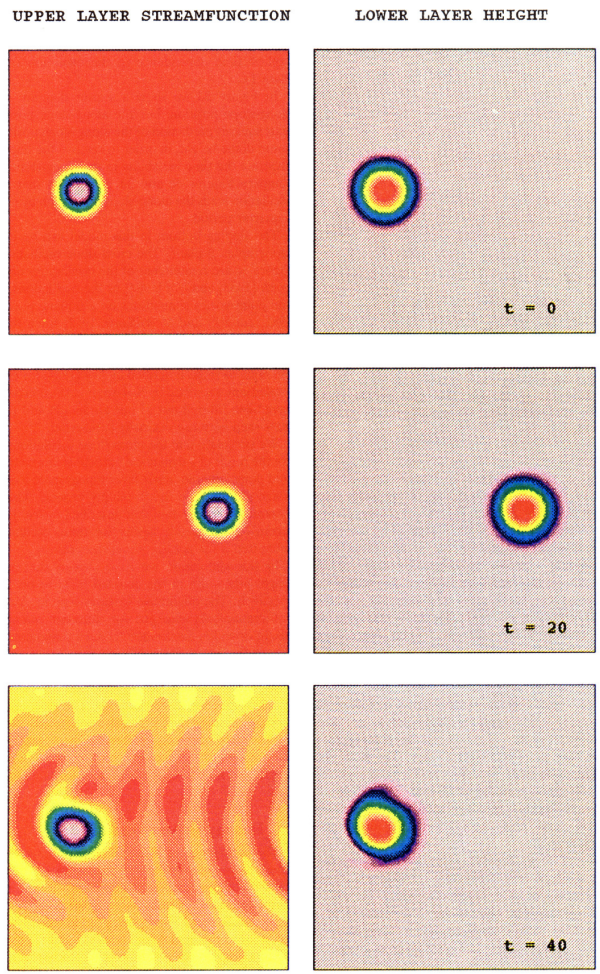

Plate 2. Sequence of panels depicting the upper layer stream function or geostrophic pressure and lower layer height for the eddy simulation which satisfies the zero topographic Rossby wave condition (27) in the upper layer initially for $t = 0$, 20, and 40, respectively. The color scale scheme and panel orientation is identical to that in Plate 1.

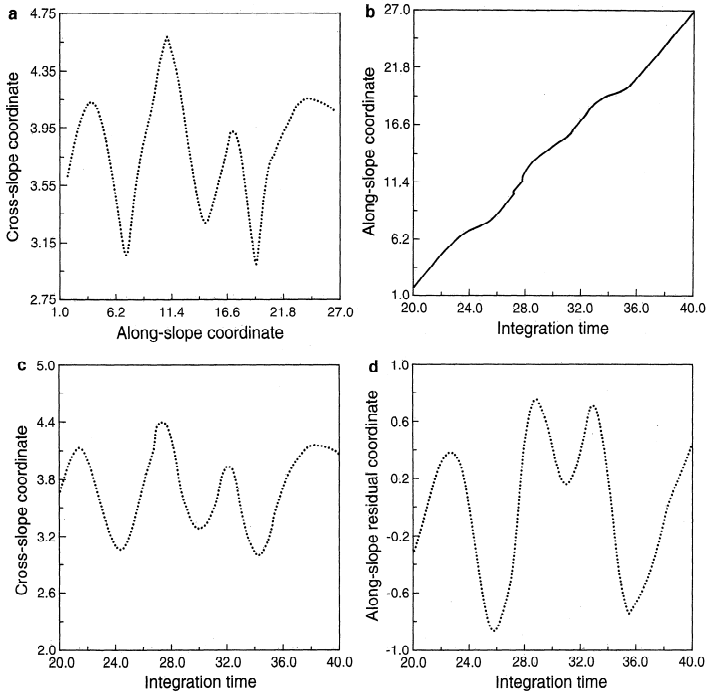

Figure 3. Scatter diagrams of (a) the cross-slope position versus the along-slope position, (b) the along-slope position, (c) the cross-slope position, and (d) the residual along-slope position (i.e., with the linear trend removed), respectively, versus the integration time of the maximum height of the lower layer dome which appears in the instability simulation from about $t = 20$ until the end of the simulation as seen in Plate 1.

where $h_B = -y$. Nof showed that all steadily traveling solutions of this model for which h has compact support (i.e., h is nonzero only over a finite area) have a translation velocity given by

$$\mathbf{c} = (c_x, c_y) = (1, 0), \qquad \left\{\mathbf{c}^* = \left(\frac{g's^*}{f_0}, 0\right)\right\} \tag{22}$$

regardless of the eddy structure.

The *Nof* [1983] solution is elegant. It predicts no cross-slope motion, and the along-slope motion is simply determined by the reduced gravity, the bottom slope, and the local Coriolis parameter. The Nof solution is completely independent of the detailed spatial structure of the fluid flow and, in particular, the vorticity field of the eddy.

One difficulty of the *Nof* [1983] solution is that it neglects the effects of baroclinicity. Presumably, as these dome structures travel through the ambient surrounding fluid there will be vortex compression/stretching and other dynamical and thermodynamical effects occurring, and these will affect the evolution of the eddy and hence its translation velocity characteristics.

For example, *Mory et al.* [1987] describe rotating tank experiments on these bottom-trapped domes. These experiments (and others, e.g., *Whitehead et al.* [1990]) clearly indicate that there was an appreciable azimuthal velocity field formed above the eddy in the surrounding eddy, which was at least as large as the swirl velocity (i.e., the azimuthal velocity in the comoving frame) in the eddy itself.

The importance of the upper layer can be seen in the Stern isolation constraint [*Mory*, 1985], which, for (1) and (2), can be expressed in the form [*Swaters and Flierl*, 1991]

$$\iint_\Omega h + \eta \, dx \, dy = 0. \tag{23}$$

This constraint, which in our context is equivalent to a zero topographic Rossby wave condition in the upper layer, must be satisfied by all isolated steadily traveling solutions to (1) and (2) or its full two-layer analogue [*Mory*, 1985]. Since $h \geq 0$ everywhere, the Stern isolation constraint clearly suggests that there must be a region of cyclonic circulation over the top of the traveling dome, and this is what is observed in the rotating tank experiments.

Nevertheless, *Swaters and Flierl* [1991] found a class of exact steadily traveling isolated eddy solutions to (1) and (2) for constant sloping topography, which travel with the *Nof* [1983] velocity. Assuming $h_B = \quad y$ and a radially symmetric eddy of the form

$$h(r) = \begin{cases} h_s(r), & 0 \leq r < a, \\ 0, & r \geq a, \end{cases} \tag{24}$$

assuming $h_s(a) = 0$, where a is the eddy radius and where r is the radial coordinate in the comoving frame, i.e., $r \equiv \sqrt{(x - t - x_0)^2 + (y - y_0)^2}$, where (x_0, y_0) is arbitrary, then η, which is the solution of

$$\Delta\eta + \eta = -h,$$

subject to the radiation condition

$$\lim_{r\to\infty} r^{1/2}\eta = 0$$

in the sector

$$\left|\tan^{-1}\left(\frac{y}{x}\right)\right| < \frac{\pi}{2},$$

is given by

$$\eta(r) = \begin{cases} \eta_s(r), & 0 \leq r < a, \\ 0, & r \geq a, \end{cases} \tag{25}$$

where

$$\eta_s(r) = -\frac{\pi Y_0(r)}{2}\int_0^r \xi J_0(\xi)h_s(\xi)\, d\xi - \frac{\pi J_0(r)}{2}\int_r^a \xi Y_0(\xi)h_s(\xi)\, d\xi, \tag{26}$$

with the zero topographic Rossby wave condition

$$\int_0^a \xi J_0(\xi)h_s(\xi)\, d\xi = 0. \tag{27}$$

These baroclinic solutions travel with the *Nof* [1983] velocity and do not exhibit any cross-slope motion. The constraint (27), which arises in order to eliminate the topographic wave field ahead of the traveling eddy in the upper layer, can be shown [*Swaters and Flierl*, 1991] to be equivalent to the Stern isolation constraint (23). It is straightforward to verify that (27) implies that $\eta_s = \eta_{s_r} = \eta_{s_{rr}} = 0$ at $r = a$.

Although there is a variational principle for these solutions, this variational principle cannot be used to examine the stability of this baroclinic eddy via an Arnol'd-like stability argument [*Swaters*, 1993]. While this failure of the Arnol'd argument to establish stability does not, of course, imply that these solutions are unstable, it is nevertheless suggestive of it. However, from a phenomenological point of view, even if these solutions are dynamical unstable, they still may have an important role in coastal ocean dynamics if the growth rates of the instabilities, if any, are long compared to the natural timescale of the eddies themselves. Thus it is of interest to numerically simulate the evolution of these (initially at least) isolated eddies.

3.1. Simulation of an Initially Isolated Dome

Here we describe the evolution of the initially smooth isolated eddy given by (24), where

$$h_s(r) = [1 + \cos(\pi r/a)]/2, \tag{28}$$

for $t = 0$ and where $\eta(r)$ is determined from (25), (26), and (27), where the integrals where numerically evaluated. The maximum initial nondimensional lower layer height is 1.0 (we will comment further on this later in this section), which is physically reasonable. For example, *Karsten and Swaters* [1996] argue that the maximum nondimensional thickness of the pulses associated with the deep water replacement current in the Strait of Georgia is about one.

The zero topographic Rossby wave condition (27) implies $a \simeq 6.85$. In addition, we choose $x_0 = -10.0$ and $y_0 = 0.0$ and solve the equations in the periodic channel domain

$$\Omega = \{(x, y) | |x| < 20, \ |y| < 20\}, \tag{29}$$

where, again, the periodicity is assumed in the x direction and $\eta = 0$ on $y = \pm 20$. The bottom topography has unit slope and is given by

$$h_B(y) = -(y + 20). \tag{30}$$

We remark that since $h_s(r)$ is continuously differentiable with respect to r, it follows from (26) that $\eta_s(r)$ is in fact 3 times continuously differentiable with respect to r. This means that the initialized Jacobian terms in (12) are continuous at the eddy boundary $r = a$. The finite difference grid used implies that initially there are 43 grid points inside the lower layer dome along the diameter.

In Plate 2 we show a sequence of color panels for the upper layer stream function and lower layer height for $t = 0$, 20, and 40. The color scale for the panels is identical to that used in Plate 1. In the $t = 0$ panel we see the initially isolated eddy. There is a pronounced cyclonic eddy immediately over the top of the dome. Within the lower layer dome the circulation is predominantly anticyclonic. There is, in fact, a small band of relatively weak cyclonic circulation adjacent to the incropping [see *Swaters and Flierl*, 1991, Figure 3a], which is required to satisfy the Stern isolation constraint.

In the $t = 20$ panel the eddy maximum is located at about $(x, y) = (9.81, -0.03)$. There appears to be very little appearance of a topographic wave field in this panel, although in the lower layer height panel, there appears to be a slowly developing azimuthal wavenumber two instability beginning to become visible. There is no discernible relative shift in the positions of the minimum in the upper layer stream function and the maximum in the lower layer height.

In the $t = 40$ panel the eddy has passed through the right-hand computational boundary and reentered the domain from the left-hand computational boundary due to the assumed along-slope periodic boundary conditions. As the eddy reenters the computational domain, it begins to interact with the previously generated topographic Rossby wave field, which acts to intensify the underlying azimuthal wavenumber two

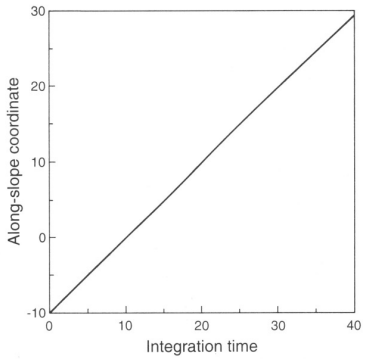

Figure 4. Graph of the along-slope position of the maximum height of the lower layer dome versus the integration time for the initially isolated eddy simulation shown in Plate 2.

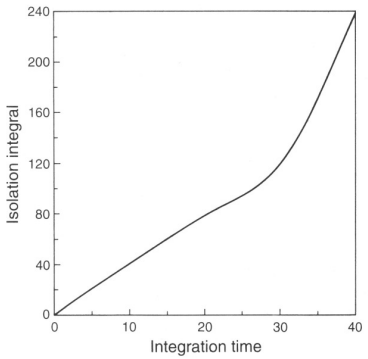

Figure 5. Graph of the value of the "isolation" integral $\int\int_\Omega h + \eta \, dxdy$ versus the integration time for the initially isolated eddy simulation shown in Plate 2.

instability in the dome, which in turn amplifies the exterior topographic Rossby wave field.

The wave field has the appearance of crescent-shaped contours which are tilted in the direction of propagation as one moves in the cross-slope direction away from the propagation path. The part of the wave field which appears to be ahead of the eddy in the $t = 40$ panel is an unfortunate consequence of using a domain which is periodic in the along-slope direction. In fact, this wave field is actually behind the propagating eddy. As shown in Figure 5 by *Swaters and Flierl* [1991], the shape of the contours arises as a consequence of the exterior topographic wave field satisfying the appropriate radiation condition upstream of the propagating eddy. In $t = 40$ panel the eddy maximum is located at about $(x, y) = (-10.91, 0.06)$. Again, there is no discernible relative shift in the positions of the minimum in the upper layer stream function and the maximum in the lower layer height.

Even though the lower layer height is beginning to deform by $t = 40$ in this simulation, it remains remarkably robust and coherent, and its propagation velocity is close to the theoretical *Nof* [1983] speed. In Figure 4 we plot the along-slope position of the maximum of the lower layer height versus the integration time as found using the quadratic interpolation procedure previously described. Here, as in Figure 3, we have added the value of the along-slope domain length (here 40) to the along-slope position as the eddy maximum height passes through the right-hand computational boundary to avoid confusion.

The curve in Figure 4 is essentially straight with very little variability. A least squares fit gave a slope of about 0.981, which is within 2% of the theoretical along-slope *Nof* [1983] velocity of 1.0. Although there was some variability in the cross-slope position of the lower layer maximum height, it did not vary much from its initial value of 0.0. Throughout the simulation the cross-slope position was contained in the interval $(-0.09, 0.07)$ and had an irregular oscillatory pattern more suggestive of numerical inaccuracies than a dynamical trend.

In Figure 5 we present a plot of the isolation integral in (23), denoted $I(t)$, given by

$$I(t) = \int\int_\Omega h + \eta \, dx \, dy, \tag{31}$$

versus integration time. As previously mentioned, *Mory* [1985] [see also *Mory et al.*, 1987] has shown that the isolation integral is necessarily zero for steadily traveling isolated eddies. Thus its departure from zero is a measure of the degree to which the traveling eddy is not isolated, i.e., the generation of an exterior wave field. In Figure 5 we see that there is a steady and almost linear increase in the value of $I(t)$ from its initial value of zero; that is, an exterior topographic Rossby field is being generated in the simulation. The sharp increase in the rate of change in $I(t)$ beginning at about $t = 30$ corresponds to the time when the eddy passes through the computational along-slope boundary, and the azimuthal wavenumber instability begins to gather momentum. We conclude that Figure 5 illustrates the fact that these initially isolated domes are (probably) not stable in a mathematical sense.

Nevertheless, these simulations suggest that these vortical structures are remarkably long-lived in comparison to the eddy circulation timescale. Indeed, for the timescalings associated with, for example, the *Houghton et al.* [1982] cold pool observations, these results suggest that these eddies can remain coherent for periods up to of the order of 250 days, which is consistent with the observations.

The last point we wish to make about this simulation concerns the possibility that fluid parcels in the upper layer can be transported by the eddy. Whether or not this occurs is a function of the maximum height of the dome in the lower layer. Upper layer fluid parcels will be transported if there are closed isolines of the comoving upper layer stream function, which, for an eddy moving with the *Nof* [1983] velocity, will be given by

$$\eta_{co} = \eta + y. \tag{32}$$

If there were no time evolution other than a steady translation, contours of η_{co} are streak lines. Even though this is not really

the case here, the numerical simulations suggest a quasi-steady translation, and thus it is appropriate, heuristically at least, to think of contours of η_{co} as streak lines.

A necessary condition for the existence of closed contours of the comoving stream function is that there exists a stagnation point in the comoving frame [e.g., *Huppert*, 1975]; that is, a point for which

$$\nabla(\eta + y) = \mathbf{0}. \tag{33}$$

Clearly, since there are coordinates for which the vector $\nabla\eta$ points in any direction because (initially at least) of the underlying radial symmetry, whether or not (33) holds is a function of the maximum initial amplitude of h since, from (26), the amplitude of η is directly and linearly related to the amplitude of h. The precise value of the maximum amplitude of h which is required to satisfy (33) is determined in part by the horizontal structure of h itself.

To illustrate the possible transport of upper layer fluid parcels associated with an initially isolated eddy, we present in Plate 3 a sequence of color panels for η_{co} and lower layer height corresponding to $t = 0$, 20, and 40 for a simulation where the initial lower layer height is given by

$$h_s(r) = 5[1 + \cos(\pi r/a)]/2, \tag{34}$$

i.e., the lower layer height had an initial maximum height of five nondimensional units, with $\eta_s(r)$ determined from (25), (26), and (27). We choose the initial maximum height to be 5.0 in order to generate an upper layer eddy with a sufficiently large region with closed η_{co}. By trial and error we found that if h_s had a maximum height larger than about 3.0, there were always regions with closed η_{co}.

A value of 5.0 for the nondimensional maximum lower layer height, while a little on the large side, is physically reasonable. For example, the *Houghton et al.* [1982] observations would suggest a maximum nondimensional height of about 2.0. The eddy radius, which is determined by (27) is, of course, unchanged. All other parameters, boundary conditions, and bottom topography in this simulation are identical to the initially isolated eddy simulation. The color scale scheme in Plate 3 is identical to that used in Plate 1.

In the $t = 0$ panel we see the initial upper layer η_{co} and lower layer height pattern. The region of closed η_{co} corresponds to the solid dark bluish region, which does not extend to the along-slope computational boundaries. The lower layer height panel is identical to the $t = 0$ height panel in Plate 2.

In the $t = 20$ panel (Plate 2) the along-slope coordinate associated with the maximum lower layer height is about 9.79. This is only about 0.02 less than the along-slope position of the maximum in the $t = 20$ lower layer height panel in Plate 2 and reflects the fact that at least up until this point in time the propagation velocity of the eddy in this simulation is well described by the *Nof* [1983] velocity.

However, the $t = 20$ η_{co} panel clearly shows the development of a topographic Rossby wave field which is larger in amplitude than that seen in the corresponding stream function panel in Plate 2. Nevertheless, there is still a region of closed η_{co}, so that fluid parcels are still being transported in the along-slope direction in the upper layer.

The $t = 20$ lower layer height panel in Plate 2 shows the initial development of a filament or plume which is beginning to propagate in the downslope direction. These features are more pronounced in this simulation compared to that in Plate 2 since the underlying instability for this eddy configuration grows faster because of the larger initial amplitude of the lower layer dome. As mentioned in the previous section, *Swaters* [1991] showed that growth rate of the most unstable mode associated with a coupled front was proportional to the maximum initial height in the lower layer. It is reasonable to suppose that this conclusion holds for an isolated eddy configuration as well.

As the eddy propagates through the right-hand computational boundary and reenters the domain from the left-hand computational boundary, it interacts with the previously developed topographic wave field, which acts to further accelerate the destabilization. Thus, as we see in the $t = 40$ lower layer height panel in Plate 2 the downslope propagating plume is substantially more developed in comparison to the corresponding panel in Plate 2. The along-slope position of the maximum lower layer height is about -14.02, which is still reasonably close to the corresponding value in the $t = 40$ panel in Plate 2 (there is an absolute difference of about 3.11 between the two positions). There does not appear to be closed η_{co} in the upper layer at this point in the simulation for the contour intervals in Plate 2. However, a high-resolution conventional (i.e., line) contour plot of η_{co} at $t = 40$ showed that there was a small region of closed η_{co}.

We conclude that along-slope transport of upper layer fluid is possible for an extended and oceanographically relevant period of time, even for a relatively unstable eddy configuration. For example, if we take the timescaling in (6) as computed from the *Houghton et al.* [1982] observations, this simulation suggests the possibility that upper layer fluid parcels can be transported for a period of time of the order of 150 days. This suggests that the baroclinic vortex structures described here may provide a mechanism for the along-continental transport of deep and intermediate water masses, which are themselves important in, for example, the meridional flux of heat and deep water propagation.

3.2. Simulation of a Nonisolated Dome

In this simulation we choose $h_s(r)$ and the domain, boundary conditions, and bottom topography to be the same as that given in the initially isolated simulation with unit maximum height (i.e., equation (28)), but here we set $\eta(x, y, 0) = 0$ to see how the dome evolves if the upper layer does not initially satisfy a zero topographic Rossby wave condition.

In Plate 4 we show a sequence of color panels for the upper layer stream function and lower layer height for the nonisolated eddy simulation for $t = 0$, 20, and 40. The color scale scheme is identical to that used in Plate 1. In the $t = 0$ panel of Plate 4 we see the radially symmetric dome in the lower layer. The lower layer panel is identical to the corresponding panel in Plate 2. The upper layer panel is blank since the stream function in the upper layer is initially assumed to be zero.

In the $t = 20$ upper layer panel we see a cyclonic eddy located over the lower layer dome. This feature develops essentially immediately after the integration begins and remains more or less uniform in amplitude and horizontal extent for much of the integration (i.e., up to about $t \simeq 30$ just before the dome propagates through the right-hand boundary).

In contrast with the $t = 20$ upper layer panel in Plate 2, there is a well developed topographic Rossby wave tail behind the traveling eddy. During the initial stages of the integration, there is a rapidly evolution of the wave field, but by $t = 20$ the

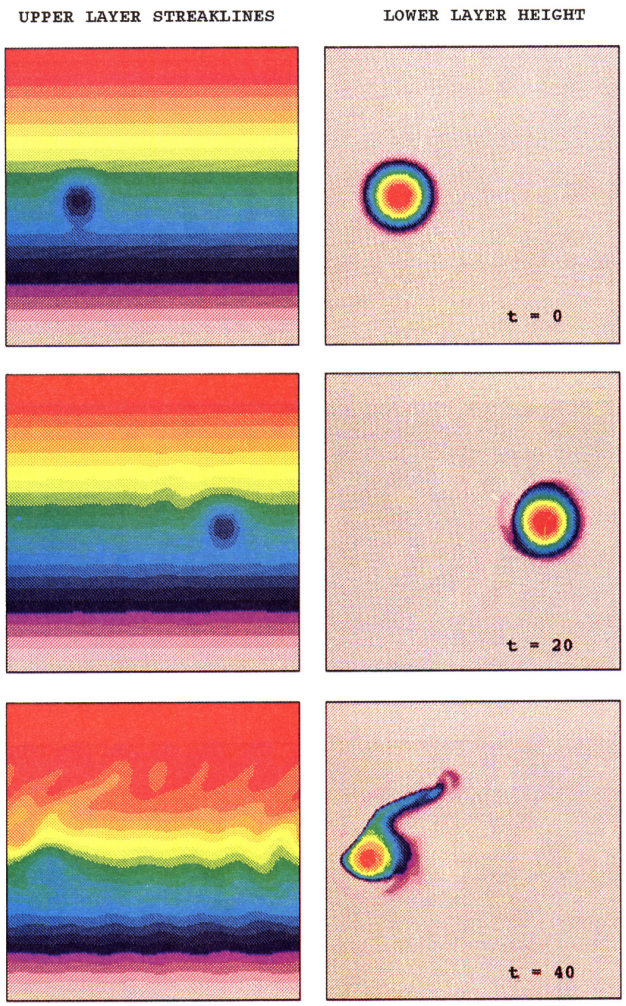

Plate 3. Sequence of panels of the comoving stream function in the upper layer given by $\eta + y$ for an initially isolated eddy with maximum height of 5.0 nondimensional units. The shaded region which does not extend to the along-slope computational boundaries contains fluid parcels which are trapped and are transported in the along-slope direction in the upper layer. The color scale scheme and panel orientation is identical to that in Plate 1.

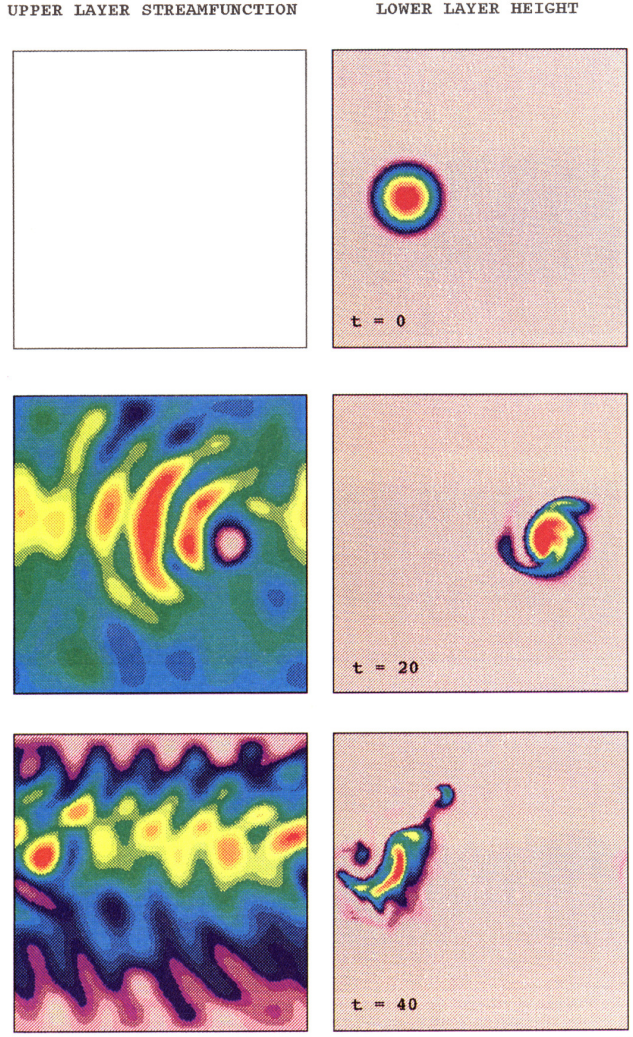

Plate 4. Sequence of panels depicting the upper layer stream function or geostrophic pressure and lower layer height for the nonisolated eddy simulation for $t = 0$, 20, and 40, respectively. The color scale scheme and panel orientation is identical to that in Plate 1.

wave field is quasi-steady in its shape until the dome propagates through the right-hand boundary. The contours associated with the wave tail are crescent shaped and tilted in the direction of propagation as one moves transversely away from the along-slope axis of propagation and qualitatively resemble the shape shown in Figure 5 by *Swaters and Flierl* [1991].

There is a clearly developing azimuthal wavenumber two instability in the lower layer dome in the $t = 20$ panel with an appearance similar to the arms in a spiral galaxy. The along-slope position of the maximum in the lower layer height field is about 8.48. This is about 1.33 units less than the position of the lower layer height field in the $t = 20$ panel in Plate 2 and reflects the effect that the upper layer topographic Rossby wave tail has on the propagation velocity of the eddy. There no discrepancy which could not be attributed to numerical inaccuracies between the position of the minimum in the upper layer stream function field and the maximum height in the lower layer.

A time series of the along-slope and cross-slope coordinates (see Figure 6) of the lower layer maximum height shows that the motion, not surprisingly, is dominated by an essentially linear along-slope component. A least squares fit of the along-slope position (see Figure 6a) of the lower layer maximum height gave a slope (i.e., an along-slope velocity) of about 0.953, which is still within 5% of the *Nof* [1983] value. We remark that as in our previous plots of the along-slope position of the maximum in the lower layer height, we added the length of the domain (here 40) to the along-slope coordinate as the dome passed through the right-hand computational boundary to make Figure 6a less confusing.

The cross-slope position of the maximum height of the dome displays (see Figure 6b) a relatively low frequency and a modest amplitude oscillation with a maximum downslope position of about 1.41 and a maximum upslope position of about -1.90. The peak-to-trough cross-slope distance of this oscillation (about 3.31 units) is only about one half an eddy radius, which initially is about 6.85 units. We interpret this cross-shelf oscillation as resulting from the interaction of the cyclonic monopole in the upper layer with the trailing topographic Rossby wave field.

In the $t = 40$ panels in Plate 4 the lower layer dome has little of its initial radial symmetry. The filaments associated with the instability have appeared to produce two smaller-scale eddies. These smaller eddies continue to propagate in the along-slope direction. In the upper layer the distinct cyclonic eddy no longer appears. The upper layer cyclonic eddy remained relatively coherent and identifiable until the lower layer dome passed through the right-hand computational boundary and reentered the domain through the left-hand computational boundary, at which point the underlying instability rapidly accelerated and the coherency was lost. However, even in this simulation, it is very interesting to observe how long the lower layer height remains more or less coherent in the numerical integration.

4. Conclusions

We have presented numerical simulations of the baroclinic dynamics of density-driven coupled fronts and eddies on a sloping bottom. Our computations are based on the *Swaters* [1991] two-layer model which filters out barotropic instability processes and focuses on the subinertial dynamics of density-driven flows on variable topography while allowing for finite-amplitude interfacial deflections in the thickness of the lower layer.

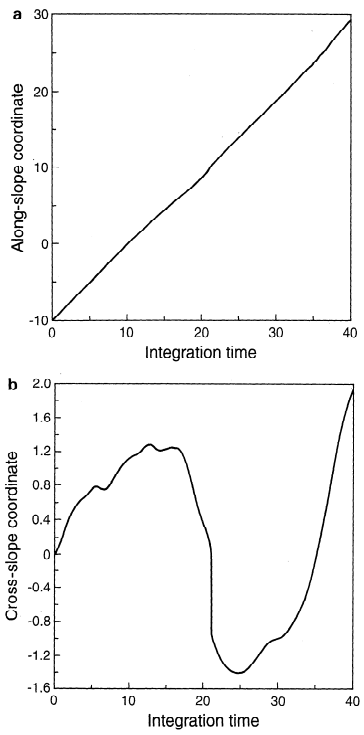

Figure 6. Plots of (a) the along-slope position and (b) the cross-slope position of the maximum in the lower layer height versus the integration time for the nonisolated eddy simulation.

The baroclinic destabilization of a coupled front was simulated. In the upper layer the instabilities take the form of amplifying topographic Rossby waves which propagate in the "westward" along-slope direction. On the coupled front the instabilities are preferentially amplified on the downslope incropping, which can be interpreted as the result of the net upslope transport of "heat" associated with baroclinic instability. This asymmetry in the amplitude of the perturbations is an unique signature of the baroclinic destabilization of a coupled front on a sloping bottom which does not occur in buoyancy-driven or surface coupled fronts. Although clearly seen in primitive equation numerical simulations [e.g., *Chapman and Gawarkiewicz*, 1995; *Gawarkiewicz and Chapman*, 1995; *Jiang and Garwood*, 1995, 1996] of overflows on continental slopes, this asymmetry, which sets apart the baroclinic instability problem for bottom-trapped coupled fronts compared to their surface-intensified counterparts, has generally not been noted previously.

The instabilities to the downslope incropping develop into downslope propagating plumes which can evolve into along-slope propagating domes in the lower layer. We analyzed the propagation characteristics of these domes and found that they traveled at an along-slope velocity which was about 20% less than the *Nof* [1983] speed. This difference can be attributed to the interaction between the dome and the surrounding topographic Rossby wave field.

The cross-slope motion of the dome was also analyzed. It exhibited an oscillatory pattern and is reminiscent of the oscillations seen in modon and point vortex simulations on a β plane [see, e.g., *Makino et al.*, 1981; *Zabusky and McWilliams*, 1982]. If the time series of the along-slope position of the maximum height of the dome has the dominant linear trend removed, the resulting residual along-slope position also exhibited an oscillatory behavior which appeared to be about 90° out of phase with the cross-shelf oscillations.

Motivated by the emergence of the isolated dome feature in the instability simulation and its possible application to cold pools observed on continental shelves [e.g., *Houghton et al.*, 1982; *LeBlond et al.*, 1991] and laboratory experiments [e.g., *Mory et al.*, 1987], we examined the propagation characteristics of initially isolated and nonisolated baroclinic eddies.

The first eddy simulation we described was for a baroclinic eddy which initially satisfies a zero topographic Rossby condition in the upper layer. These eddies correspond to a configuration in which in the lower layer the eddy height is radially symmetric, has compact support, and has, in the main, anticyclonic circulation. In the overlying layer, there is a cyclonic eddy located immediately over the lower layer dome. These solutions [see *Swaters and Flierl*, 1991] are the baroclinic analogues of the equivalent barotropic eddies discussed by *Nof* [1983]. In the absence of any additional forcing (e.g., friction or thermodynamical interactions) these eddies do not develop essentially any cross-slope motion in the course of their evolution, and their along-slope velocity remains within 2% of the *Nof* [1983] speed. There is a slowly growing azimuthal wavenumber two instability which develops on the lower layer dome with a corresponding upper layer topographic Rossby wave field, but the growth rate of the instability is long compared to the eddy timescale. Typical continental slope parameter values [e.g., *Houghton et al.*, 1982] suggest that these eddies can exist for timescales of the order 200 days.

For a sufficiently large initial height in the lower layer dome, there can exist closed comoving streamlines, which implies that these eddies can transport, in the along-slope direction, upper layer fluid as well as the water mass associated with the lower layer dome. It appears, however, that the horizontal area enclosed by the closed comoving streamlines diminishes over time as the underlying eddy instability amplifies. Nevertheless, our simulations suggest that these eddy structures can provide a mechanism for the along-continental-slope transport of bottom and intermediate waters. As such, they may have a role to play in the topographically steered meridional transport of density anomalies, which is important in deep water formation and transport.

We also discussed the evolution of eddies which do not initially satisfy a zero topographic Rossby wave condition in the upper layer. Our simulation shows that while these solutions are much more unstable than their initially isolated counterpart, a remarkable degree of coherency nevertheless remains in the lower layer dome, suggesting that even these structures can efficiently transport bottom-trapped domes. In the upper layer, there is an almost immediate development of a quasi-steady (in the comoving frame) cyclonic eddy over the top of the dome. This is accompanied by a rapidly evolving topographic Rossby wave tail behind the propagating dome. This wave tail eventually evolves into quasi-steady (in the comoving frame) configuration with crescent-shaped stream function contours similar to that computed by *Swaters and Flierl* [1991] for a diabatically heated cold pool. The motion of this dome has a modest amplitude cross-slope oscillatory drift to it with a maximal cross-slope amplitude only about one half an eddy radius. On the basis of a least squares fit of the along-slope position of the maximum eddy height in the lower layer the along-slope velocity of the eddy is still within 5% of the *Nof* [1983] speed over the course of the simulation.

It is hoped that the simulations described here will be useful in interpreting the simulations of substantially more complete numerical models [e.g., *Chapman and Gawarkiewicz*, 1995; *Gawarkiewicz and Chapman*, 1995; *Jiang and Garwood*, 1995, 1996), laboratory experiments [e.g., GKS; *Mory et al.*, 1987], and oceanographic observations [e.g., *Houghton et al.*, 1982; *LeBlond et al.*, 1991] of density-driven currents and fronts. With respect to the filtered baroclinic dynamics modeled here, there are, however, other physics we could have included but did not, i.e., along-slope topographic variability, diabatic heating of bottom-trapped domes, and bottom and horizontal friction to name a few. It will be important to understand the role that these processes play in modulating the evolution of the flows examined here.

Acknowledgments. Preparation of this manuscript was supported in part by research and equipment grants awarded by the Natural Sciences and Engineering Research Council of Canada and a science subvention awarded by the Department of Fisheries and Oceans of Canada to the author.

References

Andrews, D. G., On the existence of nonzonal flows satisfying conditions for stability, *Geophys. Astrophys. Fluid Dyn.*, *28*, 243–256, 1984.

Arakawa, A., Computational design for long term numerical integration of the equations of fluid motion: Two-dimensional incompressible flow, *J. Comput. Phys.*, *1*, 119–143, 1966.

Armi, L., and E. D'Asaro, Flow structures in the benthic ocean, *J. Geophys. Res.*, *85*, 469–483, 1980.

Asselin, R. A., Frequency filter for time integrations, *Mon. Weather Rev.*, *100*, 487–490, 1972.

Boss, E., N. Paldor, and L. Thompson, Stability of a potential vorticity front: From quasi-geostrophy to shallow water, *J. Fluid Mech.*, *315*, 65–84, 1996.

Britter, R. E., and P. F. Linden, The motion of the front of a gravity current travelling down an incline, *J. Fluid Mech.*, *99*, 531–543, 1980.

Chapman, D. C., and G. Gawarkiewicz, Offshore transport of dense shelf water in the presence of a submarine canyon, *J. Geophys. Res.*, *100*, 13,373–13,387, 1995.

Charney, J. G., and G. R. Flierl, Oceanic analogues of large-scale atmospheric motion, in *Evolution of Physical Oceanography: Scientific Surveys in Honor of Henry Stommel*, edited by B. A. Warren and C. Wunsch, pp. 504–548, MIT Press, Cambridge, Mass., 1981.

de Verdiere, A. C., On mean flow instabilities within the planetary geostrophic equations, *J. Phys. Oceanogr.*, *16*, 1981–1984, 1986.

Gawarkiewicz, G., and D. C. Chapman, A numerical study of dense water formation and transport on a shallow, sloping continental shelf, *J. Geophys. Res.*, *100*, 4489–4507, 1995.

Gibbon, J. D., I. N. James, and I. M. Moroz, An example of soliton

behavior in a rotating baroclinic fluid, *Proc. R. Soc. London A*, *367*, 219–237, 1979.
Griffiths, R. W., P. D. Killworth, and M. E. Stern, Ageostrophic instability of ocean currents, *J. Fluid Mech.*, *117*, 343–377, 1982.
Honji, H., and T. Hosoyamada, Instability of the rotating gravity current flow down a slope, *Rep. Res. Inst. Appl. Mech. Kyushu Univ.*, *XXXV*(105), 55–64, 1989.
Houghton, R. W., R. Schlitz, R. C. Beardsley, B. Butman, and J. C. Chamberlin, The middle Atlantic bight pool: Evolution of the temperature structure during 1979, *J. Phys. Oceanogr.*, *12*, 1019–1029, 1982.
Huppert, H. E., Some remarks on the initiation of inertial Taylor columns, *J. Fluid Mech.*, *67*, 397–412, 1975.
Jiang, L., and R. W. Garwood Jr., A numerical study of three-dimensional dense bottom plumes on a Southern Ocean continental slope, *J. Geophys. Res.*, *100*, 18,471–18,488, 1995.
Jiang, L., and R. W. Garwood Jr., Three-dimensional simulations of overflows on continental slopes, *J. Phys. Oceanogr.*, *26*, 1214–1233, 1996.
Karsten, R. H., and G. E. Swaters, Nonlinear stability of baroclinic fronts in a channel with variable topography, *Stud. Appl. Math.*, *96*, 183–199, 1996.
Karsten, R. H., G. E. Swaters, and R. E. Thomson, Stability characteristics of deep-water replacement in the Strait of Georgia, *J. Phys. Oceanogr.*, *25*, 2391–2403, 1995.
Killworth, P. D., On the motion of isolated lenses on a beta-plane, *J. Phys. Oceanogr.*, *13*, 368–376, 1983.
LeBlond, P. H., and L. A. Mysak, *Waves in the Ocean*, Elsevier, New York, 1978.
LeBlond, P. H., H. Ma, F. Doherty, and S. Pond, Deep and intermediate water replacement in the Strait of Georgia, *Atmos. Ocean*, *29*, 288–312, 1991.
Makino, M., T. Kamimura, and T. Taniuti, Dynamics of two-dimensional solitary vortices in a low-β plasma with convective motion, *J. Phys. Soc. Jpn.*, *50*, 980–989, 1981.
Mooney, C. J., and G. E. Swaters, Finite-amplitude baroclinic instability of a mesoscale gravity current in a channel, *Geophys. Astrophys. Fluid Dyn.*, *82*, 173–205, 1996.
Mory, M., Integral constraints on bottom and surface isolated eddies, *J. Phys. Oceanogr.*, *15*, 1433–1438, 1985.
Mory, M., M. E. Stern, and R. W. Griffiths, Coherent baroclinic eddies on a sloping bottom, *J. Fluid Mech.*, *183*, 45–62, 1987.
Nof, D., The translation of isolated cold eddies on a sloping bottom, *Deep Sea Res., Part A*, *30*, 171–182, 1983.
Nof, D., Oscillatory drift of deep cold eddies, *Deep Sea Res., Part A*, *31*, 1395–1414, 1984.
Paldor, N., and P. D. Killworth, Instabilities of a two-layer coupled front, *Deep Sea Res., Part A*, *34*, 1525–1539, 1987.
Pedlosky, J., The equations for geostrophic flow in the ocean, *J. Phys. Oceanogr.*, *14*, 448–455, 1984.
Pedlosky, J., *Geophysical Fluid Dynamics*, 2nd ed., Springer-Verlag, New York, 1987.
Smith, P. C., Baroclinic instability in the Denmark Strait overflow, *J. Phys. Oceanogr.*, *6*, 355–371, 1976.
Stacey, M. W., S. Pond, P. H. LeBlond, H. J. Freeland, and D. M. Farmer, An analysis of the low-frequency current fluctuations in the Strait of Georgia, from June 1984 until January, 1985, *J. Phys. Oceanogr.*, *17*, 326–342, 1987.
Stacey, M. W., S. Pond, and P. H. LeBlond, An objective analysis of the low frequency currents in the Strait of Georgia, *Atmos. Ocean*, *26*, 1–15, 1988.
Stacey, M. W., S. Pond, and P. H. LeBlond, Flow dynamics in the Strait of Georgia, British Columbia, *Atmos. Ocean*, *29*, 1–13, 1991.
Swaters, G. E., On the baroclinic instability of cold-core coupled density fronts on a sloping continental shelf, *J. Fluid Mech.*, *224*, 361–382, 1991.
Swaters, G. E., Nonlinear stability of intermediate baroclinic flow on a sloping bottom, *Proc. R. Soc. London A*, *442*, 249–272, 1993.
Swaters, G. E., and G. R. Flierl, Dynamics of ventilated coherent cold eddies on a sloping bottom, *J. Fluid Mech.*, *223*, 565–587, 1991.
Warn, T., and P. Gauthier, Potential vorticity mixing by marginally unstable waves at minimum shear, *Tellus, Ser. A*, *41*, 115–131, 1989.
Whitehead, J. A., and L. U. Worthington, The flux and mixing rates of Antarctic Bottom Water within the North Atlantic, *J. Geophys. Res.*, *87*, 7903–7924, 1982.
Whitehead, J. A., M. E. Stern, G. R. Flierl, and B. Klinger, Experimental observations of a baroclinic eddy on a sloping bottom, *J. Geophys. Res.*, *95*, 9585–9610, 1990.
Zabusky, N. J., and J. C. McWilliams, A modulated point vortex model for geostrophic, β-plane dynamics, *Phys. Fluids*, *25*, 2175–2182, 1982.
Zoccolotti, L., and E. Salusti, Observations on a very dense marine water in the southern Adriatic Sea, *Cont. Shelf Res.*, *7*, 535–551, 1987.

G. E. Swaters, Department of Mathematical Sciences, 632 Central Academic Building, University of Alberta, Edmonton, Alberta T6G 2G1, Canada. (e-mail: gordon.swaters@ualberta.ca)

(Received February 21, 1997; revised June 30, 1997; accepted August 28, 1997.)